The International Journal of Advanced Manufacturing Technology (2024) 132:5367–5383
https://doi.org/10.1007/s00170-024-13665-x

ORIGINAL ARTICLE

Optimal ovoid lobe shape by an automatic calculation program and CFD using dynamic mesh technique

Chanyoung Shin[1] · Seungseok Lee[1] · Chul Kim[1]

Received: 20 November 2023 / Accepted: 18 April 2024 / Published online: 2 May 2024

Abstract
The gerotor oil pump is advantageous for miniaturization as it can deliver a higher output per rotation compared to pumps of the same size and finds wide application in hydraulic systems such as engine lubrication and automatic transmission systems due to its low noise and superior suction performance. It was observed that increasing the chamber width leads to better pulsation and noise performance. High pressure pulsation is a significant factor in vibration and noise generation in oil pumps, particularly crucial for electric vehicles where quietness is emphasized. A previously developed profile was not used in electric vehicles due to this problem. To compensate for this problem, the characteristics of flow and noise according to the area of the chamber were found, and the rotor was designed and analyzed to minimize the pressure pulsation and noise level by applying this. The internal and external rotors were designed based on the ovoid parameter equations, incorporating rotation, translational motion, and expansion algorithms. The designed profile was applied to a GUI and an automatic performance factor calculation program in MATLAB to derive the optimal profile with the best performance. To test the performance of the developed profile, computational fluid dynamics (CFD) using the dynamic mesh technique and experiment was conducted. These design techniques can be used to create and test various gerotor profiles that meet various design requirements, and to develop a pump with improved performance, reduced noise, and improved efficiency while satisfying various design requirements and maintaining miniaturization and reliability.

Keywords Gerotor · Oil pump · Computer-aided design · Profile design · Optimization · Ovoid · Performance · Irregularity · Noise

1 Introduction

The gerotor oil pump is a type of internal gear pump consisting of an outer gear and an inner gear, forming a rotor set. The outer gear is typically located around the inside perimeter of the pump housing, while the inner gear meshes with the outer gear and rotates. This rotating rotor set is responsible for sucking in and discharging oil, facilitating oil circulation within the engine. This device is a simple molded product with a structure that is easy to manufacture, and it can be used for an extended period due to minimal friction occurring as the gears mesh. Moreover, the gerotor oil pump exhibits relatively small size, high flow rates, and high pressure capabilities, making it suitable for high-performance engines. The gerotor oil pump is used not only in automotive engines but also in various fields such as machine tools, robots, and hydraulic equipment. To address issues in the automotive industry, such as fuel efficiency improvement and noise reduction, there is still a demand for new gerotor pump designs with high performance and low noise characteristics, as well as port optimization.

The works above focus on comprehensively exploring innovative solutions to improve the performance of the gerotor oil pump, solving lubrication and leakage problems, optimizing fluid flow through geometric design changes, and reducing noise and pressure pulsations [1]. These studies range from developing a sealing magnetic rotor for miniaturization and efficiency to using elliptical configurations to improve fluid dynamics, to theoretical and computational

✉ Chul Kim
chulki@pusan.ac.kr

Chanyoung Shin
cksdud9488@naver.com

Seungseok Lee
dltmdtjr311@gmail.com

[1] School of Mechanical Engineering, Pusan National University, 2, Busandaehak-ro 63beon-gil, Geumjeong-gu 46241, Busan, Republic of Korea

analysis to optimize pump design and function. Each contribution emphasizes the importance of integrating advanced design concepts and interpretation methodologies to achieve excellent performance in the gerotor oil pump. Lee's research introduced a gerotor oil pump with a 2-extended cardioid lobe shape, and Lee optimized the gerotor profile using a lemniscate lobe shape [2, 3]. The results from both studies show that the narrower the width of the chamber of the gerotor, the lower the flow rate pulsation and the better the noise. Based on these results, the relationship between the flow pulsation, pressure pulsation, and noise according to the gear shape was derived by referring to Zhang's research result on the pressure pulsation and flow structure, and a gerotor tooth shape with improved performance compared to the previous one was developed [4–6].

In order to meet the recent demand for gerotor oil pumps with low pulsation and noise values, a new gerotor profile was developed through the following process [7].The ovoid curve was chosen as the basis for the lobe shape design. Based on the designed lobe shape, the constitutive equation of the gear profile was derived. To effectively validate the theoretical performance parameters of the developed gerotor profile, an automated calculation program was developed using Matlab to compute performance factors, including flow rate, pulsation, contact stress, specific slipping, and pressure angle. In addition, a CFD method using a dynamic mesh was established to perform more accurate analytical verification of the generated tooth shape. By this method, the optimal shape of the ovoid profile was derived, and it was confirmed that its performance is superior to the lemniscate profile developed in previous research. Through this, the correlation between the area and performance of the flow area was confirmed and the optimal shape of the ovoid profile was derived by this, and it was confirmed that the theoretical and analytical performance was superior to that of the lemniscate profile developed in the previous study. After obtaining promising results through CFD analysis, an experiment was conducted to test the performance, and as a result, it was confirmed the excellence of the ovoid rotor robe, especially in terms of flow rate and noise reduction. This result confirms the correlations between the chamber width and noise, flow rate pulsation and noise, and pressure pulsation and noise, paving the way for the development of a pump that offers improved performance, reduced noise, and enhanced efficiency. This advancement meets diverse design requirements while ensuring compactness and reliability.

2 Profile design

2.1 Lobe shape

In previous studies, it was found that pulsation and noise performance were better when the chamber width was relatively wide. From this point of view, in order to create a tooth shape that outperforms existing profiles and to find out why the performance is improved, a trial and error method was performed to obtain an ovoid curve with a wider chamber width than the existing curve as shown in Fig. 1, and the tooth shape of the gerotor was designed using this [8–10].

Ovoid curves are egg-shaped curves that can be represented by various parametric equations. In this study, the optimal design of the gerotor tooth profile was carried out using the parametric equations shown in Eqs. (1) and (2). A 2-expanded ovoid curve was designed to generate a lobe shape through scaling, translation, rotation, and symmetry algorithms, and the process of creating a lobe shape is as follows.

$$x_1(\theta) = \left(\sqrt{49 - 4\sin(\theta)} + \cos(\theta)\right)\cos(\theta) \tag{1}$$

$$y_1(\theta) = \sin(\theta) \tag{2}$$

To achieve this, it was expanded by k_1 times in the x-direction and k_2 times in the y-direction. The expanded ovoid curve was created based on Eq. (3) and is shown in Fig. 2.

$$x_2(\theta) = k_1 \times x_1,\ y_2(\theta) = k_2 \times y_1 \tag{3}$$

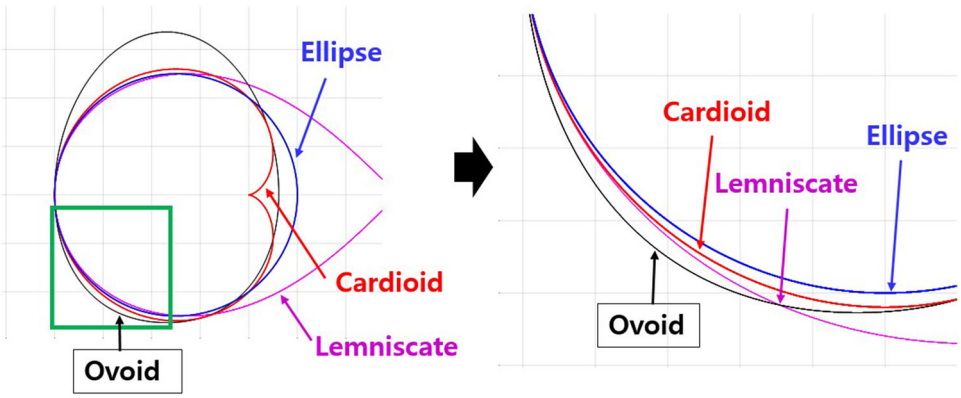

Fig. 1 Differences between curvature of ovoid curve and those of other curves

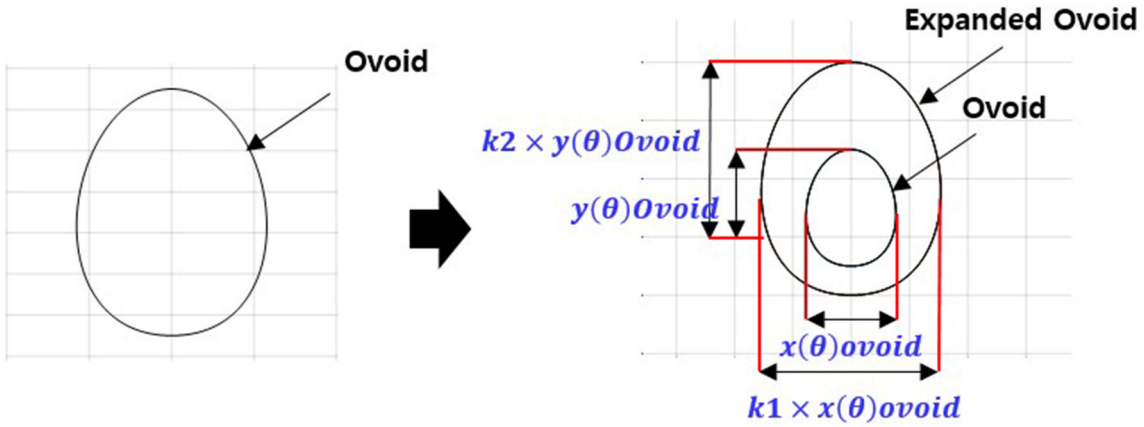

Fig. 2 Ovoid and expanded ovoid curves

It was translated parallel to the x-axis by an amount equal to "x_{move}," and parallel to the y-axis by an amount equal to "y_{move}," reaching the origin as shown in Fig. 3. Subsequently, it was rotated around the origin, which serves as the center of rotation, by an angle of "$\eta°$." The resulting configuration iss shown by blue in Fig. 3 and the parametric equations are shown in Eq. 4.

$$\begin{aligned} x_{3,\text{rotated}}(\theta) &= (x_2 - x_{\text{move}})\cos(\eta) - (y_2 - y_{\text{move}})\sin(\eta) \\ y_{3,\text{rotated}}(\theta) &= (x_2 - x_{\text{move}})\sin(\eta) + (y_2 - y_{\text{move}})\cos(\eta) \end{aligned} \tag{4}$$

When the ovoid curve is symmetrical to the x-axis and combined, a cusp occurs. When a cusp occurs, a discontinuity appears in the rotor shape, so smooth rotation does not occur and flow pulsation and flowrate are affected (Fig. 4).

To prevent this, a point with a slope of "∞" in the rotated lobe shape was found and connected to form a natural curve.

As shown by purple in Fig. 5, we translated the point with the minimum x-coordinate by "x_{move2}" in the x-axis direction and by "h" in the y-axis direction. The lobe shape becomes an independent curve having various shapes according to "k_1," "k_2," and the rotation angle "η" and its parametric equations of the extended ovoid curve are shown in Eqs. 5, 6, and 7.

$$\begin{aligned} x_4(\theta) &= x_{3,\text{rotated}}(\theta) \\ &= (x_2 + x_{\text{move}}) \times \cos(\eta) - (y_2 - y_{\text{move}}) \times \sin(\eta) \\ &= \Big[\Big\{ k_1 \times \Big((\sqrt{49 - 4 \times \sin(\theta)} + \cos(\theta)) \times \cos(\theta) \Big) \Big\} \\ &\quad + x_{\text{move}} \Big] \times \cos(\eta) - \{ k_2 \times (\sin(\theta) - y_{\text{move}}) \} \times \sin(\eta) \\ y_{4,Y\text{-translation}}(\theta) &= y_{3,\text{ rotated}}(\theta) - \text{h} \\ &= (x_2 + x_{\text{move}}) \times \sin(\eta) + (y_2 - y_{\text{move}}) \times \cos(\eta) - \text{h} \\ &= \Big[\Big\{ k_1 \times ((\sqrt{49 - 4 \times \sin(\theta)} + \cos(\theta)) \times \cos(\theta)) \Big\} \\ &\quad + x_{\text{move}} \Big] \times \sin(\eta) + \{ k_2 \times (\sin(\theta) - y_{\text{move}}) \} \times \cos(\eta) - \text{h} \end{aligned} \tag{5}$$

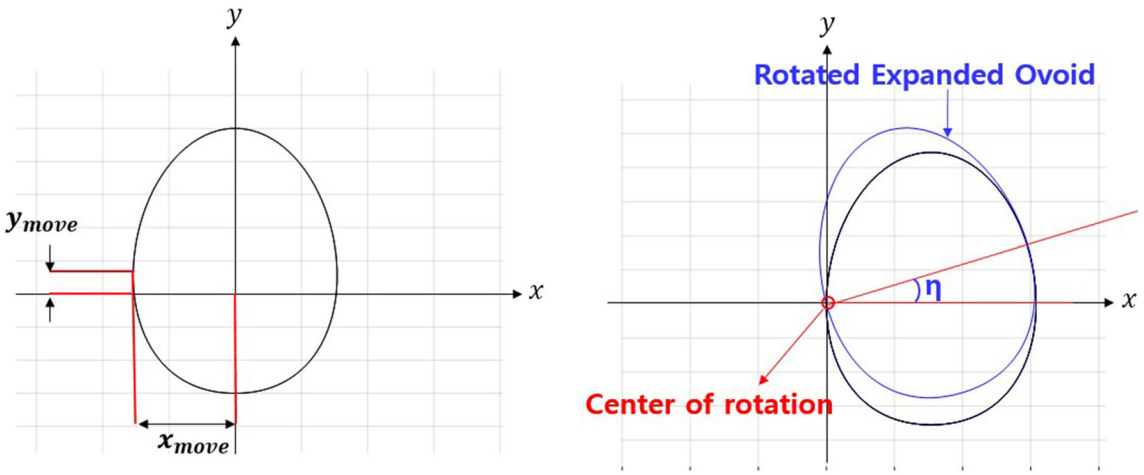

Fig. 3 Movement and rotation of the Ex_Ovoid curve

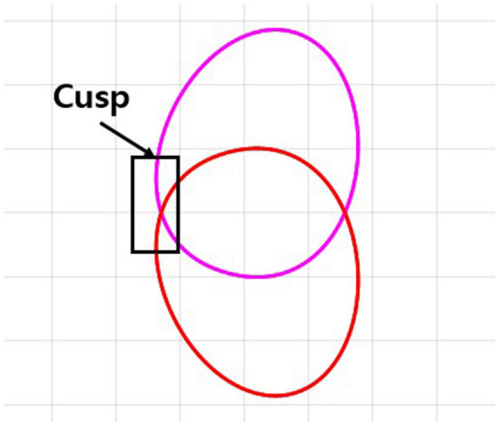

Fig. 4 Occurrence of cusp when rotated around the x-axis

$$\begin{aligned} x_{5,X\text{-translation}}(\theta) &= x_{4,\text{ translation}} + x_{\text{move},2} \\ y_{5,X\text{-translation}}(\theta) &= y_{4,\text{ translation}} \end{aligned} \tag{6}$$

$$\begin{aligned} x_6(\theta) &= x_{5,X} - \text{ translation} \\ y_{6,\text{ symmetry}}(\theta) &= -y_{5,X\text{-translation}} \end{aligned} \tag{7}$$

To determine the position of this shape, they were translated parallel to the x-axis by a distance of "d," using Eq. (8). Afterwards, in order to obtain the final lobe shape of Fig. 6, Eq. (8) was symmetric about the x-axis, which are shown in Eq. (9).

$$\begin{aligned} x_{7-1,x\text{-translation}}(\theta) &= x_{5,x\text{-translation}} + d \\ &= \left\{\left[k_1 \times \left(\sqrt{49 - 4 \times \sin(\theta)} + \cos(\theta)\right) \times \cos(\theta)\right] \right. \\ &\quad \left. + x_{\text{move}}\right\} \times \cos(\eta) - \{k_2 \times \sin(\theta) \times \sin(\eta)\} \\ &\quad + x_{\text{move},2} + d \\ y_{7-1}(\theta) &= y_{5,x\text{-translation}}(\theta) \\ &= \left[\sqrt{49 - 4 \times \sin(\theta)} + x_{\text{move}}\right] \times \sin(\eta) \\ &\quad + \{k_2 \times \sin(\theta) \times \cos(\eta)\} - h \end{aligned} \tag{8}$$

$$\begin{aligned} x_{7-2,X-translation}(\theta) &= x_{7-1}(\theta) \\ y_{7-2}(\theta) &= -y_{7-1}(\theta) \end{aligned} \tag{9}$$

2.2 Contact points

To create gears that mesh with a constant angular velocity ratio using the obtained lobe shape, we applied Camus' theory. According to this theory, the common normal at the contact point of the meshing teeth must always pass through the pitch point, which is a fixed point on the gear centerline.

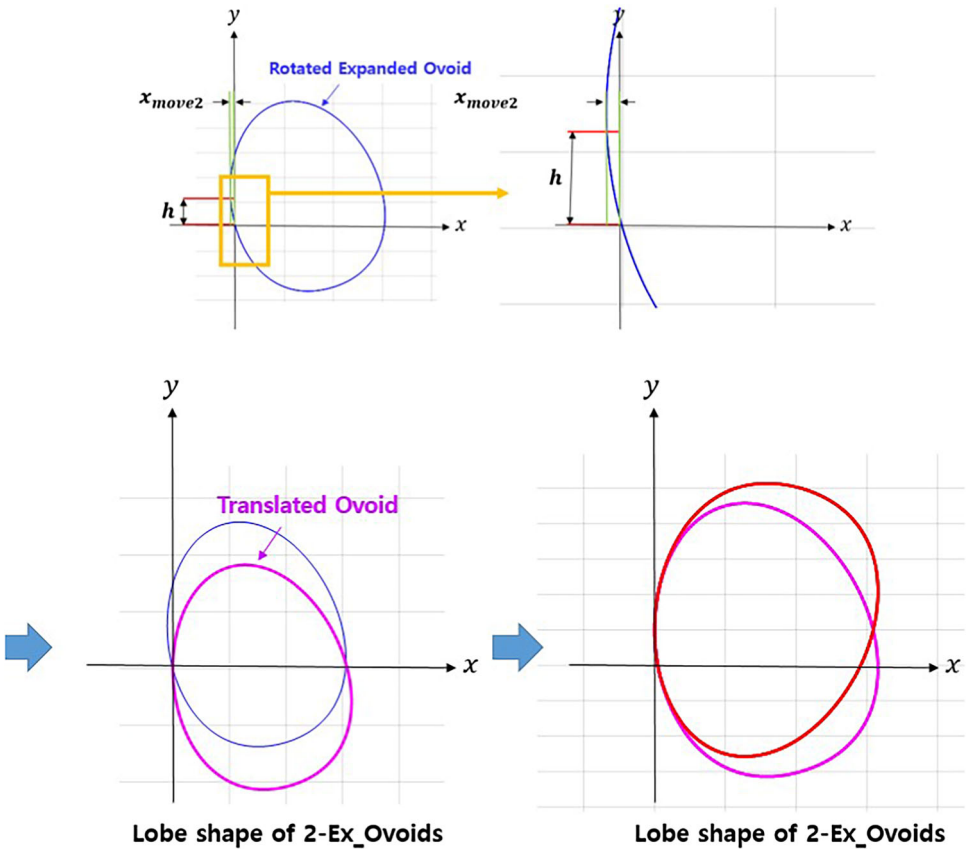

Fig. 5 The 2-Ex_Ovoids lobe shape designed through mirror function to avoid cusp

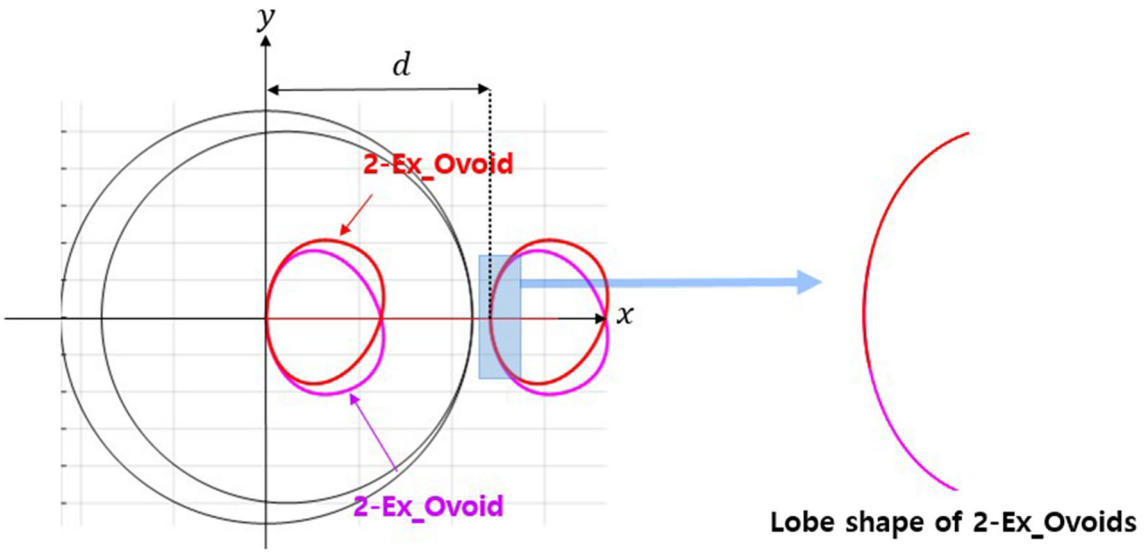

Fig. 6 Generation of the 2-Ex_Ovoids lobe shape

Unlike the case where the external profile is a circle, in the case of a rotor profile composed of two combined expanded ovoid curves, the normal at the contact point does not point towards the center of the external gear. Therefore, as shown in Fig. 7, using the Newton–Raphson method, we found the angle (η°) between the direction vector ($\vec{v}_1$) from a point (x_1, y_1) on the rotor to the pitch point P(P_x, P_y) and the tangent vector ($\vec{v}_2$) to be perpendicular, satisfying an error range within 10^{-7}. Then, we calculated the contact points C_1 and C_2 of the expanded ovoid curves 1 (2-Ex_Ovoid1) and 2 (2-Ex_Ovoid2) using Eqs. (10)–(14), and represented them in Fig. 8.

In this case, Eq. (10) represents the pitch point of the external rotor, and Eq. (11) defines "$\vec{v}_1$" as the direction vector from a point on the rotor to the pitch point, and "$\vec{v}_2$" as the normal vector at that point on the rotor. Equation (12) represents the condition that "$\vec{v}_1$" and "$\vec{v}_2$" are perpendicular.

$$P\left(P_x, P_y\right) = \left(r_2 \cos\alpha, r_2 \sin\alpha\right) \tag{10}$$

$$\overrightarrow{v_{n,1}} = \left(P_x - x_n, P_y - y_n\right), \overrightarrow{v_{n,2}} = \left(dx_n, dy_n\right) \tag{11}$$

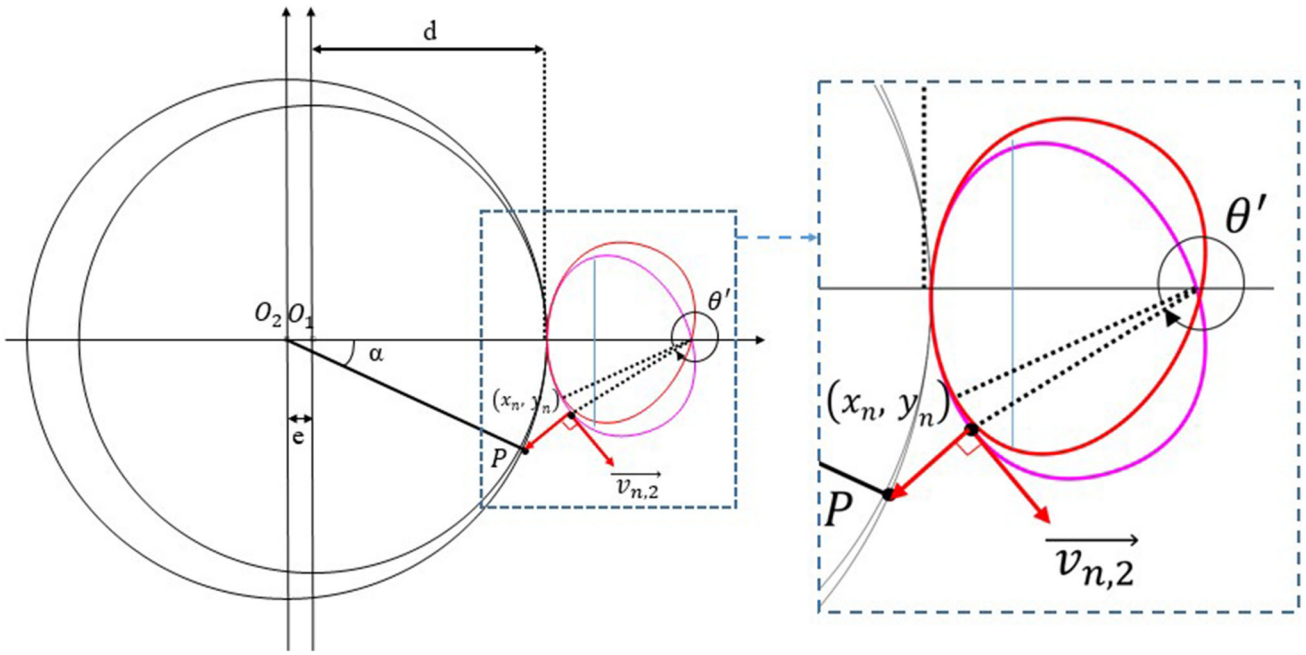

Fig. 7 Contact points obtained by orthogonal condition

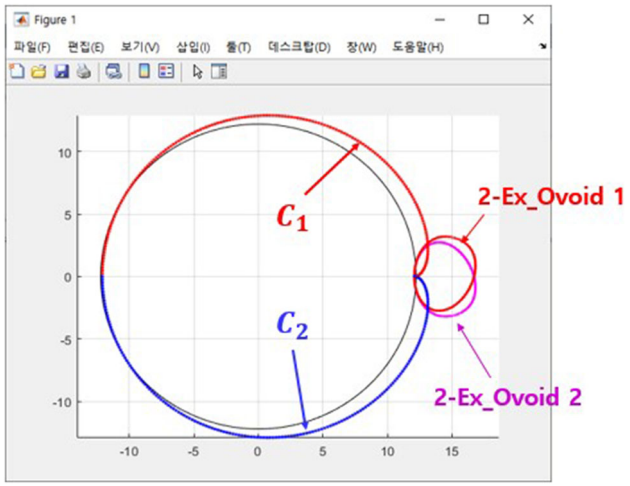

Fig. 8 Locus of contact points of the 2-Ex_Ovoids

$$ff = \overrightarrow{v_{n,1}} \cdot \overrightarrow{v_{n,2}} = 0 \tag{12}$$

$$\theta' = \theta - \frac{ff}{dff} \tag{13}$$

$$\mathrm{C} = \begin{pmatrix} x_c \\ y_c \end{pmatrix} = \begin{pmatrix} x_7(\theta') \times \cos(\alpha) - y_7(\theta') \times \sin(\alpha) \\ x_7(\theta') \times \sin(\alpha) + y_7(\theta') \times \cos(\alpha) \end{pmatrix} \tag{14}$$

2.3 Design of inner and outer rotors

Using Eqs. (15)–(17), the contact point (x_c, y_c) is rotated clockwise by "α'" based on the center point (O_1) of the inner rotor to create the inner rotor (x_{inner}, $y$inner), and the contact point External rotors (x_{outer}, y_{outer}) are created by rotating clockwise by "α'" based on the center point (O_2) of the outer rotor. "r_1" and "r_2" represent the pitch circle radius of the inner and outer rotors, and "e" represents the amount of eccentricity.

$$\alpha' = \frac{r_2}{r_1}\alpha, \ (r_1 = z_1 \times e, r_2 = z_2 \times e) \tag{15}$$

$$\begin{pmatrix} x_{\text{inner}} \\ y_{\text{inner}} \end{pmatrix} = \begin{pmatrix} \cos\alpha' & -\sin\alpha' \\ \sin\alpha' & \cos\alpha' \end{pmatrix} \begin{pmatrix} x_c - e \\ y_c \end{pmatrix} + \begin{pmatrix} e \\ 0 \end{pmatrix} \tag{16}$$

$$\begin{pmatrix} x_{\text{outer}} \\ y_{\text{outer}} \end{pmatrix} = \begin{pmatrix} \cos\alpha & -\sin\alpha \\ \sin\alpha & \cos\alpha \end{pmatrix} \begin{pmatrix} x_c \\ y_c \end{pmatrix} \tag{17}$$

Figure 9 shows the shape of the inner and outer rotors created when the input variables (k_1 = 5, k_2 = 6, η = 15, d = 15) were entered. Various rotor shapes can be generated through a combination of these input variables.

The tooth profile shown in Fig. 9 is changing by the values of each design variable ("k_1," "k_2," and "η"). As shown in Fig. 10, as the value of "k_1" increases, the lobe shape expands in the x-axis direction, and the root part of the external rotor is widely generated, and as the value of "k_2" increases, the

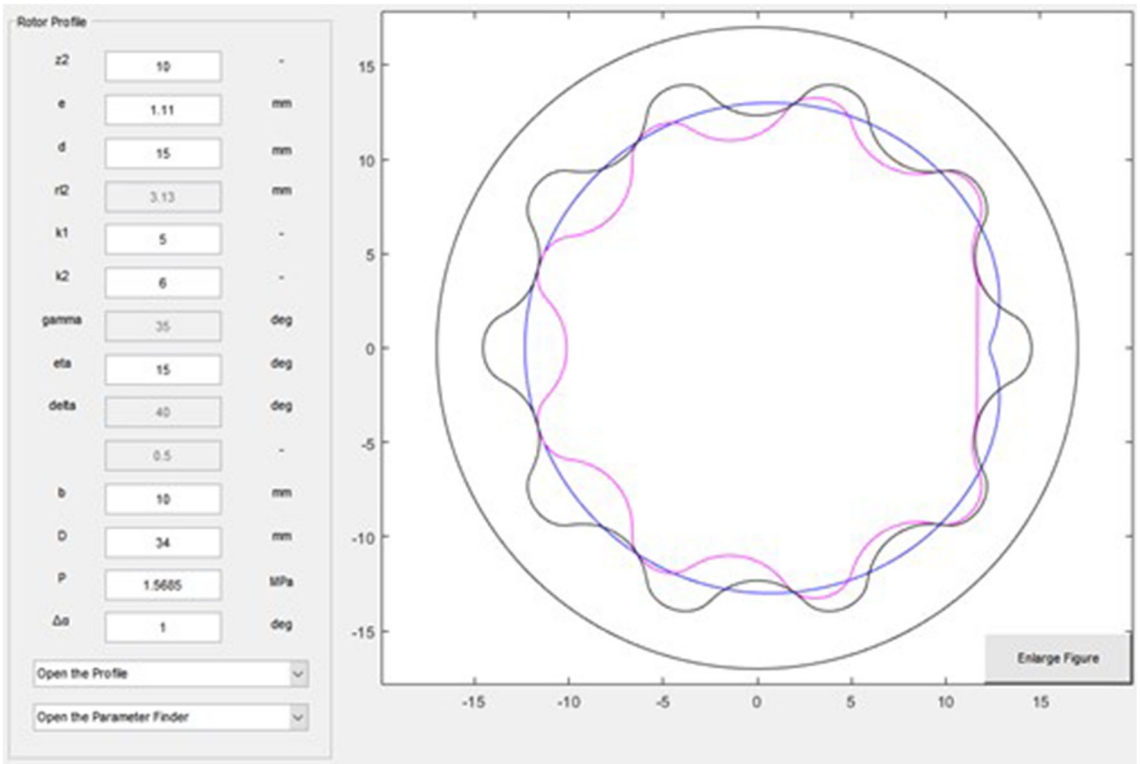

Fig. 9 Generated inner and outer rotor profiles

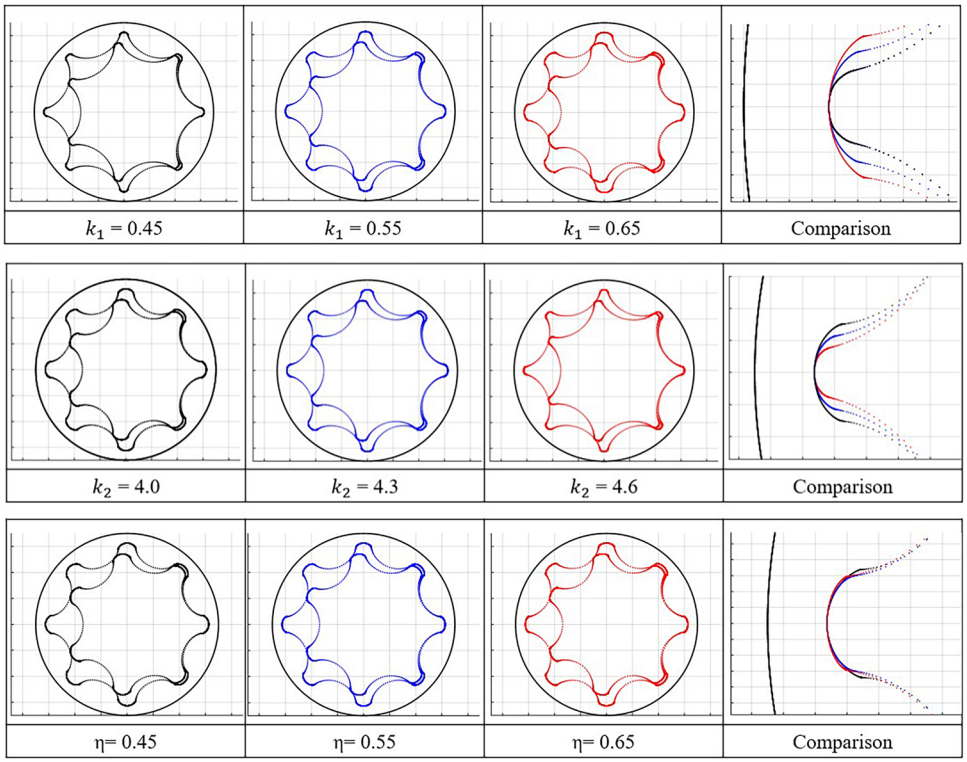

Fig. 10 Shape change according to each design variable

lobe shape expands in the y-axis direction, and the root part of the external rotor is formed narrowly. The curvature of the rotor changes as the value of "η" changes.

3 Process for designing and testing optimal georotor geometry

3.1 Theoretical performance of gerotor

The flow rate (Q) of the gerotor can be calculated using Eq. (15). "$A_{\max}$" and "$A_{\min}$" are the maximum and minimum areas of the chamber, and "b," "ρ_{fluid}," and "ω" are the thickness of the rotor, the density of the hydraulic fluid, and the rotational speed of the inner rotor, respectively. As shown in Eq. 19, the flow irregularity (i) is the value obtained by dividing the average area (q_{average}) by the difference between the maximum area ($q_{\max}$) and the minimum area ($q_{\min}$) of the chamber.

$$Q = Z_1 \left(A_{\max} - A_{\min}\right) \rho_{\text{fluid}}\, b\omega_1 \tag{18}$$

$$i = \frac{q_{\max} - q_{\min}}{q_{\text{average}}} \tag{19}$$

The specific sliding is the ratio of the sliding speeds in the plane crossing the contact point between the two meshing gears. It is the difference between the tangential rolling speed on the tooth and the speed normal to the line of action. Equation (20) shows the calculation equations of the sliding rates (ss_1 and ss_2)) of the inner and outer rotors, where "v_1" and "v_2" are the sliding speeds of the inner and outer rotors, respectively.

$$ss_1 = \frac{|v_1 - v_2|}{v_1}, \qquad ss_2 = \frac{|v_2 - v_1|}{v_2} \tag{20}$$

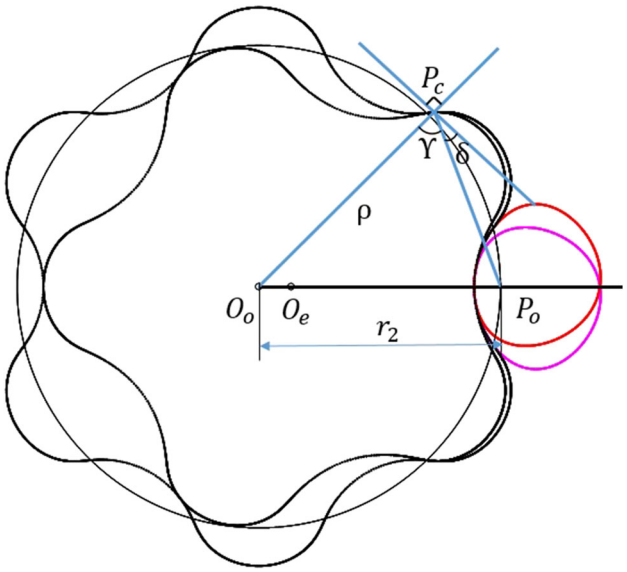

Fig. 11 Schematic model of pressure angle

As shown in Fig. 11, the pressure angle (ω) is the angle between the common tangent of gears meshing at the pitch circle and the common normal of the contacting teeth and is calculated from Eqs. (21)–(22).

$$\gamma = \cos^{-1}\left(\frac{\rho^2 + P_c\bar{P}_o{}^2 - r^2}{2P_c\bar{P}_o\rho}\right) \tag{21}$$

$$\delta = 90^\circ - \gamma \tag{22}$$

The contact stress (P_H) of two objects in relative motion is calculated by the Hertzian contact stress equation shown in Eq. 23. "F" is the contact force applied to the inner rotor at the contact point, "E" is the elastic modulus of the rotor, "b" is the tooth width, "R" is the equivalent radius of curvature, and "ρ_i" and "ρ_o" are the inner rotor and the radius of curvature of the outer rotor (Fig. 12).

$$P_H = \sqrt{\frac{FE}{2\pi bR}}, \quad R = \left(\frac{1}{\rho_i} + \frac{1}{\rho_o}\right)^{-1} \tag{23}$$

3.2 Development of automatic calculation program

The contact stress (P_H) of two objects in relative motion is calculated by the Hertzian contact stress equation shown in Eq. 23. "F" is the contact force applied to the inner rotor at the contact point, "E" is the elastic modulus of the rotor, "b" is the tooth width, "R" is the equivalent radius of curvature, and "ρ_i" and "ρ_o" are the inner rotor and the radius of curvature of the outer rotor. Using MATLAB (R2020b, The MathWorks, Inc. Natick, MA, USA), a commercial numerical analysis software, a graphical user interface (GUI), and performance factor multi-calculation program were developed to generate an optimal ovoid tooth shape.

The GUI consists of an input module (lobe shape selection and design parameter) and an output module (generated profile and performance factors). When design parameters are entered in the input module, internal and external rotor shapes are generated in the output module, and performance factors (flow rate, flow irregularity, contact stress, specific sliding, pressure angle) and minimum outer rotor radial thickness calculations are automatically output on the screen. The range of design factors that meet the performance conditions required by the field was derived after the tooth was generated according to the specifications of the tooth shape.

A multiple calculation program developed using MATLAB is shown in Fig. 13. This program operates by inputting the range and spacing of design variables obtained from the GUI as shown in Fig. 13(a). And based on various combinations of these design variables, the process of generating the tooth shape described above is repeated. Through this, a number of profiles are generated to satisfy the minimum tooth thickness, minimum flow rate, and contact stress criteria as shown in Fig. 13(b).

The performance factor for each tooth profile generated through this process is calculated and the calculated data is stored. Teeth profiles that do not satisfy the specified conditions are filtered, and the performance factor is not calculated. Subsequently, as shown in Fig. 13(b), the design factor and performance factor calculation results for each tooth profile can be summarized. At this time, each performance factor value corresponding to the top 10% is marked for flow irregularity, contact stress, specific sliding, and pressure angle. After that, the entire profile is aligned according

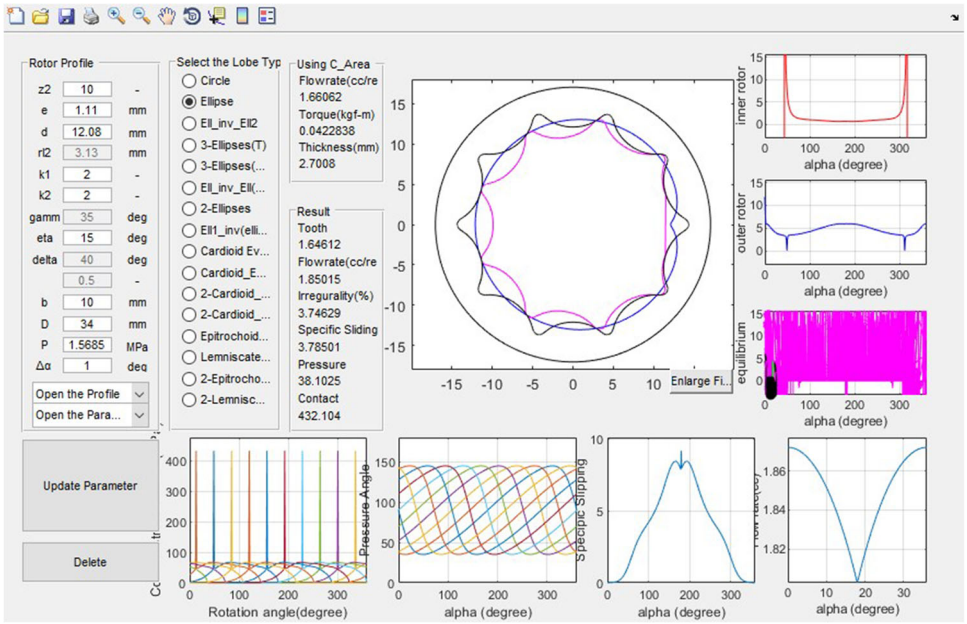

Fig. 12 Matlab GUI for automatic gerotor design

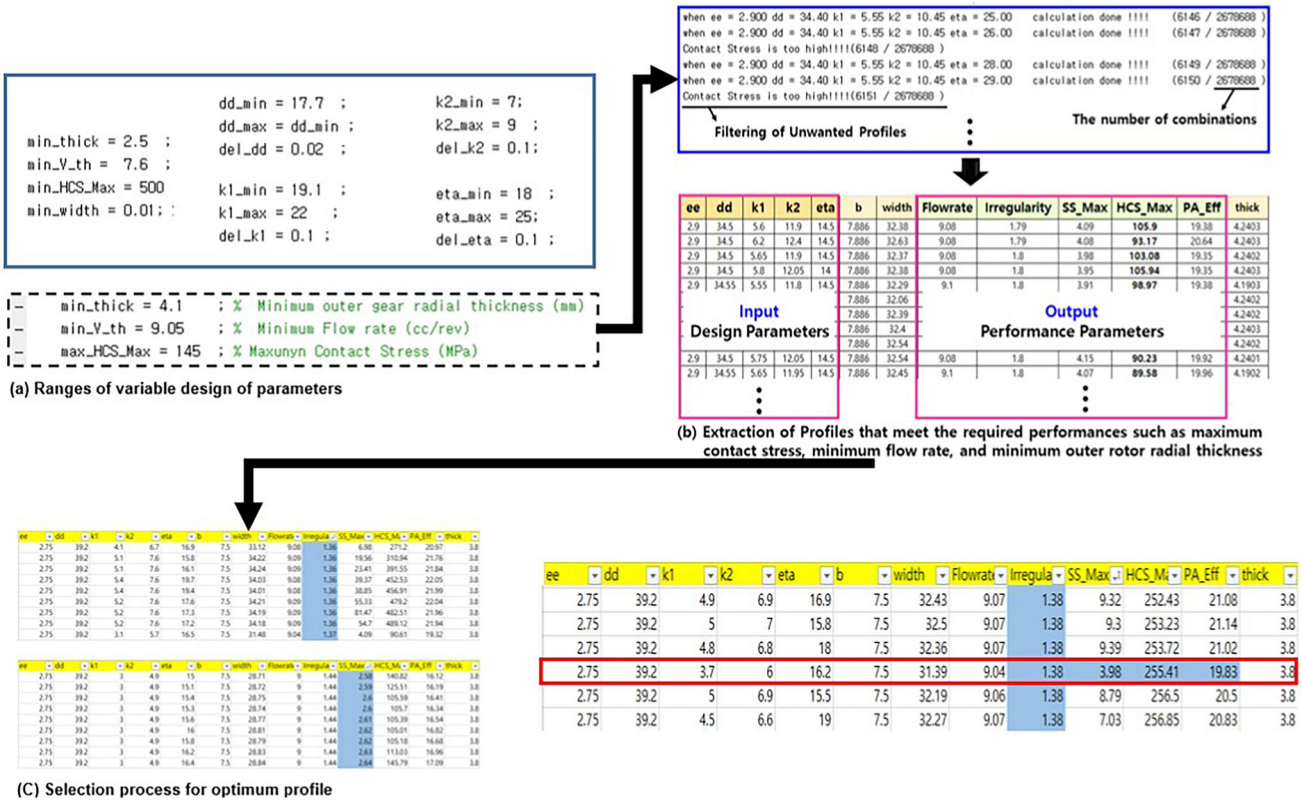

ee	dd	k1	k2	eta	b	width	Flowrate	Irregularity	SS_Max	HCS_Max	PA_Eff	thick
2.75	39.2	4.9	6.9	16.9	7.5	32.43	9.07	1.38	9.32	252.43	21.08	3.8
2.75	39.2	5	7	15.8	7.5	32.5	9.07	1.38	9.3	253.23	21.14	3.8
2.75	39.2	4.8	6.8	18	7.5	32.36	9.07	1.38	9.39	253.72	21.02	3.8
2.75	39.2	3.7	6	16.2	7.5	31.39	9.04	1.38	3.98	255.41	19.83	3.8
2.75	39.2	5	6.9	15.5	7.5	32.19	9.06	1.38	8.79	256.5	20.5	3.8
2.75	39.2	4.5	6.6	19	7.5	32.27	9.07	1.38	7.03	256.85	20.83	3.8

Fig. 13 The design parameter results carried out in the multiple calculation program

to the priority of the performance factors (flow irregularity > contact stress > specific sliding > pressure angle), and the tooth shape marked with all four performance factors is selected as the optimal tooth.

3.3 CFD using dynamic mesh method

For CFD analysis, a commercial program Fluent from Ansys was used, and the analysis was performed by applying the dynamic mesh technique [11]. As shown in Fig. 14, the gerotor has a different rotational axis of the inner rotor and outer rotor, making it difficult to set the rotational axis of the chamber, which is an empty space inside. In general, modeling is performed so that the outer rotor and the inner rotor, which are solid areas, overlap with the chamber, which is a fluid area as Fig. 14.

However, in this case, the velocity streamline is measured in the solid area as shown in Fig. 15, this analysis model does not reflect the actual phenomenon and has poor accuracy. Additionally, when measuring pressure pulsations, as shown in Fig. 16, the measurements often deviate significantly, being either too high or too low, and they do not exhibit the periodicity.

Therefore, analysis using a dynamic mesh technique was conducted. This technique involved removing both the outer rotor and inner rotor from the model, focusing solely

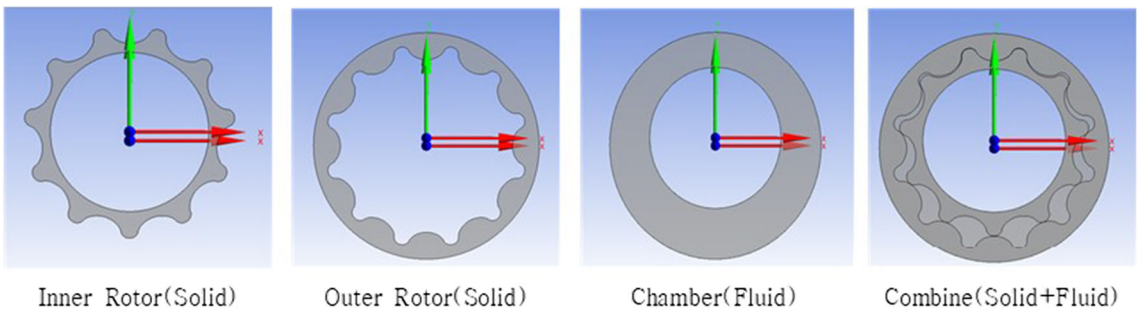

Fig. 14 Analysis model existed

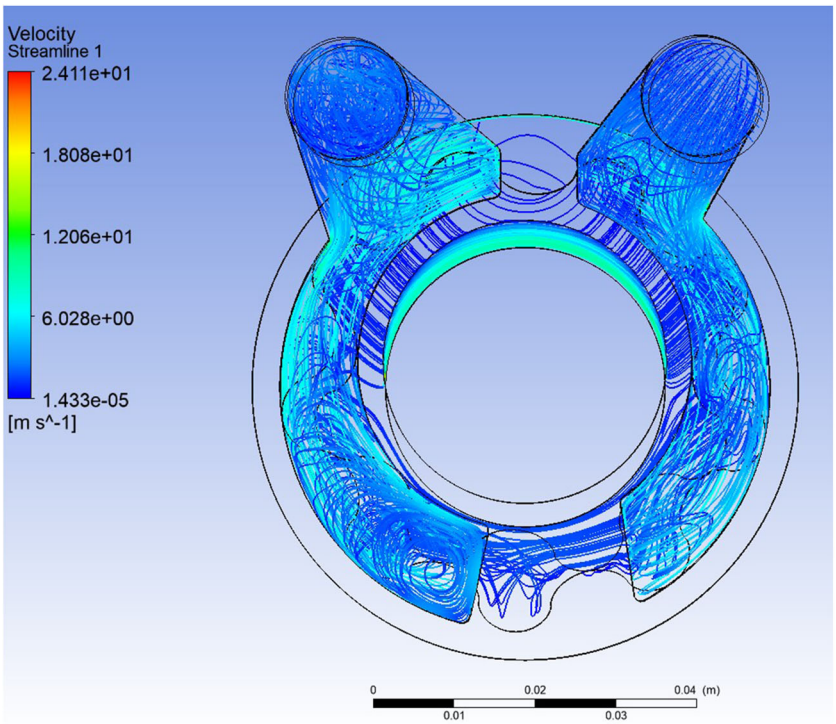

Fig. 15 Velocity streamline measured in the solid region

on modeling the chamber located between them. In this approach, only the boundary of the rotor was allowed to rotate, as depicted in Fig. 17. Dynamic mesh is a technique that promotes interface changes in the model over time, and adjusts the mesh shape near the interface to induce mesh deformation and subsequent regeneration. Accordingly, a grid within the computational area that changes continuously due to the rotation of the two gears is synchronized with the rotation of the gears and automatically reproduced at each computational time step.

In Fluent, mesh regeneration according to boundary surface change can be controlled by using the smoothing method and remeshing method. When the motion displacement or rotation of an object is large, low-quality grid cells based on the volume or skewness conditions of the grid are locally regenerated (remeshing) if necessary. On the other hand, when the movement of an object is small, a local smoothing technique is used. In this case, the nodes move and change in size to improve the quality of the cell, but the connectivity is maintained. The smoothing method is a setting to prevent mesh quality deterioration such as mesh distortion and entanglement that can affect the accuracy and convergence of simulation results. Among them, Diffusion was used, which moves mesh nodes in response to the displacement of the boundary by calculating the mesh velocity using the diffusion equation Eq. (24). "$\vec{u}$" is the mesh displacement velocity and "γ" is the diffusion coefficient. Equation (25) or (26) is applied to "γ," respectively, depending on the case of boundary distance formulation and cell volume formulation.

$$\nabla \cdot (\gamma \nabla \mathbf{u}) = 0 \tag{24}$$

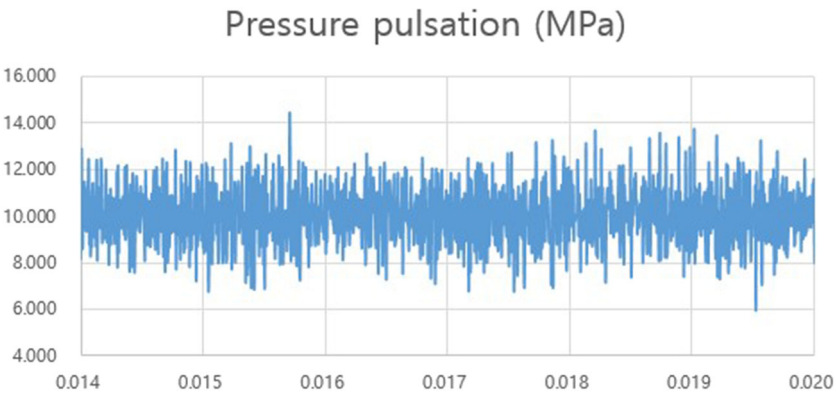

Fig. 16 Pressure pulsation measured by general method

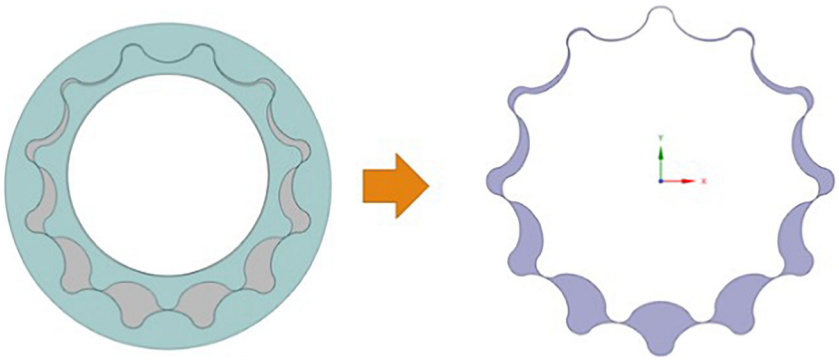

Fig. 17 Modified analysis model to apply dynamic mesh

$$\gamma = \frac{1}{a\alpha} \tag{25}$$

$$\gamma = \frac{1}{\mathbf{V}} \tag{26}$$

The remeshing method is a function that regenerates the mesh based on the updated geometry when the mesh's quality is degraded due to changes in the mesh due to fluid flow or mechanical motion. Among them, local remeshing, local face remeshing, and region face remeshing were used. Considering the deformation size and analysis time of the mesh, the minimum length was set to 0.1 mm and the maximum length was set to 0.5 mm.

UDF (user-defined function) was used to simulate the rotational motion of the gear. Rotational speed of 2666.67 and 3000 rpm, respectively, was input so that the interface between the inner rotor and the outer rotor could rotate at a constant speed ratio. In order to give the rotational speed to the interface between the inner and outer rotors, it was matched according to each axis of rotation in the Dynamic Mesh Zones setting.

When applying the remeshing technique, the relative speed is caused by the movement of the mesh interface in the initially configured CFD mesh cell unit, and the conservation equation needs to be corrected. The conservation Eq. (27) in any control volume is expressed below (V) where the boundary moves with respect to the dynamic mesh.

$$\frac{d}{dt}\int_V \rho\phi dV + \int_{\partial V} \rho\phi(\vec{u} - \vec{u_g})\cdot d\vec{A} = \int_V \Gamma\nabla\phi\cdot d\vec{A} + \int_V S_\phi dV \tag{27}$$

"ρ" refers to the density of the fluid, "$\vec{u}$" refers to the fluid velocity vector, "$\vec{u_g}$" refers to the lattice velocity vector, "Γ" refers to the diffusion coefficient, "S_θ" refers to the source term of "θ," and "∂V" refers to the boundary of the control volume.

Using the first-order backward difference formula, the time differential term can be expressed as Eq. (28). Here, "n" and "n+1" mean the present and next time steps, and the volume "V^{n+1}" in the "n+1" time steps is calculated as Eq. (29). Here, "dV/dt" means the time difference of the control volume, and is calculated as Eq. (30) to satisfy the law of conservation of the grid.

$$\frac{d}{dt}\int_V \rho\phi dV = \frac{(\rho\phi V)^{n+1} - (\rho\phi V)^n}{\Delta t} \tag{28}$$

$$V^{n+1} = V^n + \frac{dV}{dt}\Delta t \tag{29}$$

$$\frac{dV}{dt} = \int_{\partial V} \vec{u}_g \cdot d\vec{A} = \sum_f \vec{u}_{g,j}\cdot\vec{A}_j \tag{30}$$

In the above equation, n_f represents the number of faces of the control volume, and "$\vec{A}_j$" represents the area vector of the j-th surface. For each control volume plane, the right term of Eq. (27) is calculated by Eq. (31).

$$\frac{d}{dt}\int_V \rho\phi dV = \frac{3(\rho\phi V)^{n+1} - 4(\rho\phi V)^n + 4(\rho\phi V)^{n-1}}{2\Delta t} \tag{31}$$

Since it was confirmed that the ovoid gerotor is superior to lemniscate in theoretical performance factors, CFD with a dynamic mesh was used to verify this. The model of the pump was built by Autodesk Inventor. A 2D drawing obtained as a function of geometric parameters was extruded to generate a gear profile. An assembly of the volume and port inside the gear was used to extract the surface of the fluid area. A view of the entire fluid model is illustrated in Fig. 18. The pressure in the area shown in the picture was measured.

The continuous Eq. (31) and the Navier–Stokes Eq. (33) were used as governing equations in the simulation.

$$\frac{\partial U_i}{\partial x_i} = 0 \tag{32}$$

$$U_j\frac{\partial U_i}{\partial x_j} + \frac{\partial(\overline{u_i u_j})}{\partial x_j} + \frac{\partial p}{\partial x_i} - \frac{1}{Re}\nabla^2 U_i = 0 \tag{33}$$

For analysis, a pressure base solver was applied in a transient state. For the turbulence model, the standard k-ε model

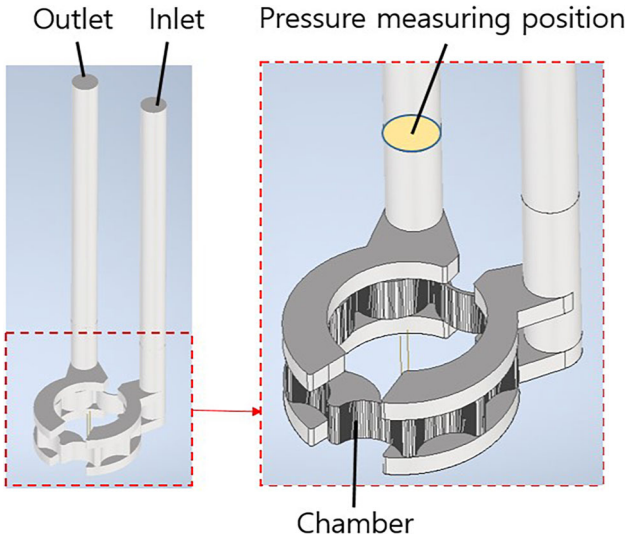

Fig. 18 Full analysis model and pressure measurement location

was used. The governing equations of fluid flow systems are augmented by the integration of two complementary transport equations that serve to characterize the turbulent properties of the flow. The first is an equation for the turbulent kinetic energy (k). It tracks turbulent energy and is used to model the transport and dissipation of energy. The second is the equation for the dissipation rate (ε). Within the framework of the two-equation turbulence model, the velocity scale and length scale are addressed separately, each with its own transport equation Eqs. (34) and (35).

$$\frac{D(\rho k)}{Dt} = \frac{\partial}{\partial x_j}\left[\left(\mu + \frac{\mu_t}{\sigma_k}\right)\frac{\partial k}{\partial x_j}\right] + \mu_t S^2 - \rho\varepsilon \tag{34}$$

$$\frac{D(\rho \varepsilon)}{Dt} = \frac{\partial}{\partial x_j}\left[\left(\frac{\mu + \mu_t}{\sigma_\varepsilon}\right)\frac{\partial \varepsilon}{\partial x_j}\right] + \frac{\varepsilon}{k}(C_{\varepsilon 1}\mu_t S^2 - \rho C_{\varepsilon 2}\varepsilon) \tag{35}$$

Oil, a working fluid, is regarded as an incompressible fluid and its physical properties are listed in Table 1. Calculations were performed at intervals of 2.4×10^{-6}s considering the rotational speed of the rotor (3000 RPM). The boundary conditions in the analysis are shown in Table 2.

To simulate the rotational motion of a gear using a user-defined function (UDF) written in C language, the following steps were followed. In order for the boundary surfaces of the inner and outer rotors to rotate at a constant speed ratio, the rotation speed information of 2666.67 rpm and 3000 rpm was input, respectively, according to the gear ratio. To apply this rotation speed information to the boundary surfaces of the inner and outer rotors, an appropriate matching was performed through the Dynamic Mesh Zones setting, and the rotation axis was defined. In addition, it was set to allow the rotating surface and the adjacent surface to deform together.

As a result of the analysis, it was confirmed that the velocity component occurred only inside the flow field as intended and showed a flow tendency closer to the actual situation. The measurement result of the velocity component is shown in Fig. 19.

Table 1 Material property of working fluid)

Working fluid	Density (kg/m^3)	Absolute viscosity (Pa·s)
Oil	799.7	0.66×10^{-2}

Table 2 Material property of working fluid

Software	Ansys Fluent 2021 R2
Solver	Transient state
Working fluid	Oil
Turbulence model	Standard k-ε (standard wall function)
Interface	Mesh interface
scheme	Coupled
Flux type	Momentum based
Inlet pressure (P_i)	0 bar
Outlet pressure (P_o)	10 bar
Temperature	85°C

4 Selection of optimal tooth profiles with 2-ovoid lobe shape

4.1 Selection of optimal tooth shape through automatic performance factor calculation program

Through the process developed as described above, the optimal gerotor (9/10, external diameter 34 mm, external diameter 2.7 mm, and thickness 10 mm) was selected as follows. Based on previous research [12], considering the priority of the effect of performance factors on noise, two extended ovoid optimal tooth shapes for noise reduction were selected ("d'' = 12.0325mm, "k1" = 0.5, "k2" = 4.4, "η" =

Table 3 Comparison of performance parameters of optimal gerotors (2-Ex_Lemniscates and 2-Ex_Ovoids)

Lobe type	2-Ex_Lemniscates	2-Ex_Ovoids
Irregularity (%)	3.88	3.86 (0.52%↓)
Contact stress (MPa	156.46	150.34 (5.8%↓)
Specific sliding	3.06	4.31 (1.25↑)
Pressure angle (degree)	20.51	24.11 (3.6°↑)
Flow rate (cc/rev)	3.39	3.45 (1.7%↑)

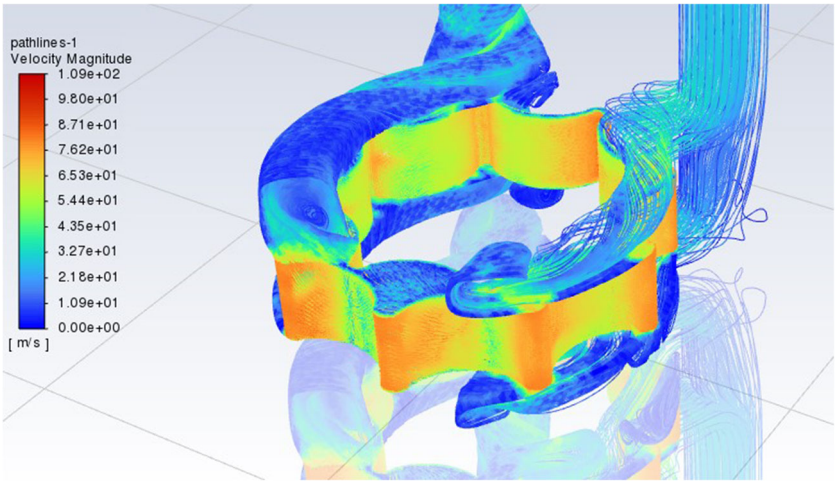

Fig. 19 Velocity magnitude for dynamic mesh application model

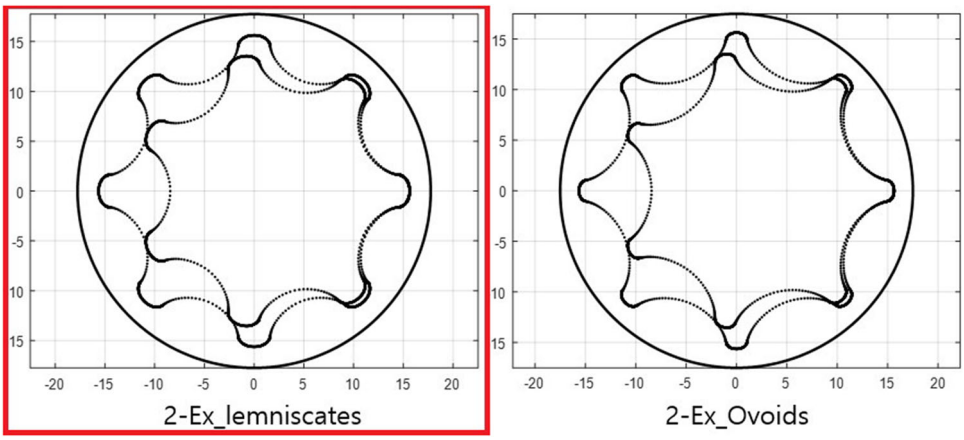

Fig. 20 Optimal gerotor profile selected by the multiple calculation program

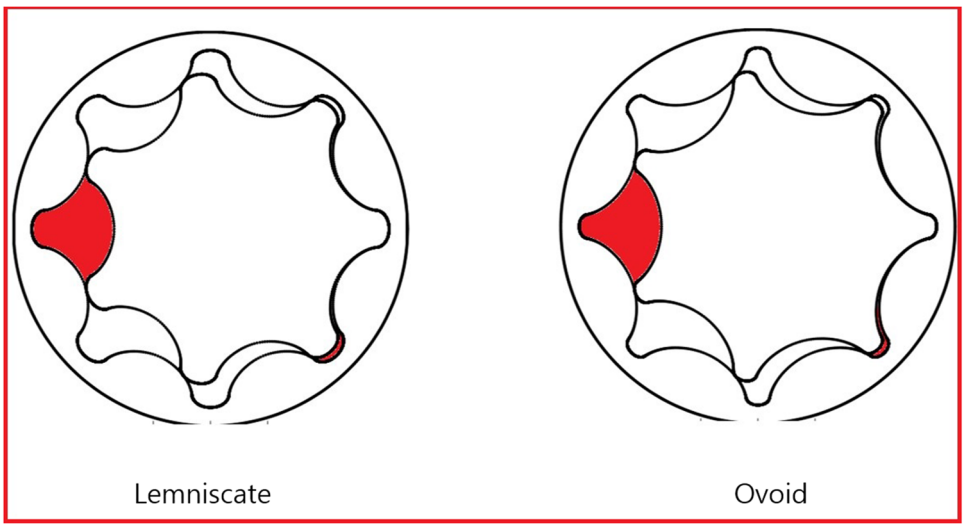

Fig. 21 Differences in the flow area of the internal volume

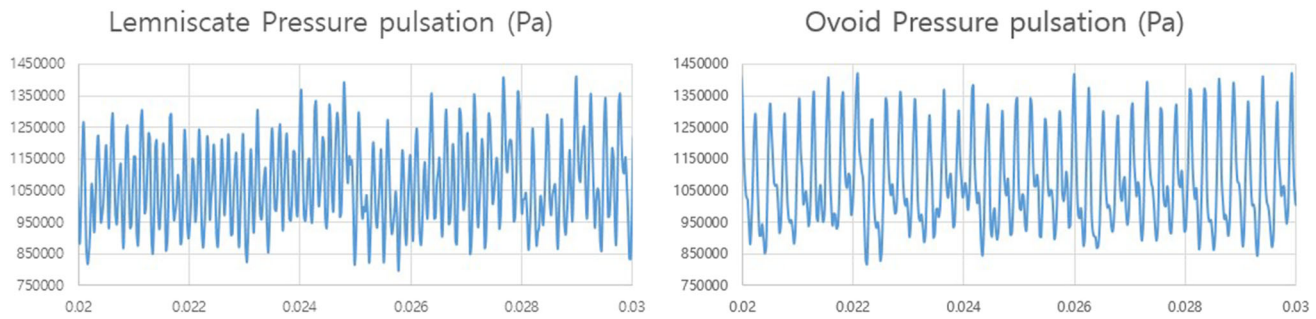

Fig. 22 Comparison of pressure pulsation between two types

Fig. 23 Comparison of volticity magnitude between two types

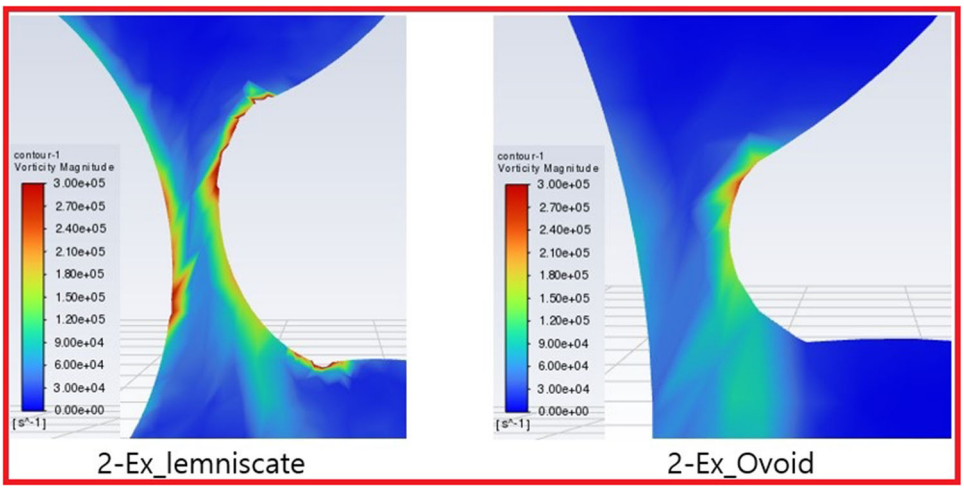

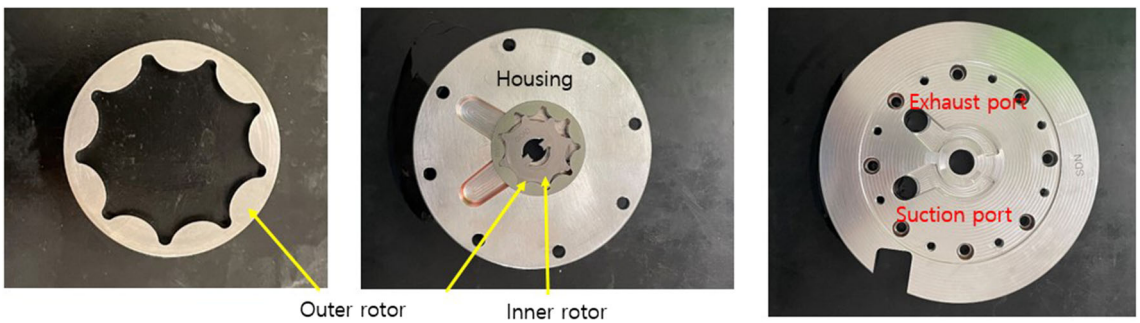

Fig. 24 Prototype of the oil pump with the optimal gerotor with the 2-Ex_Ovoids

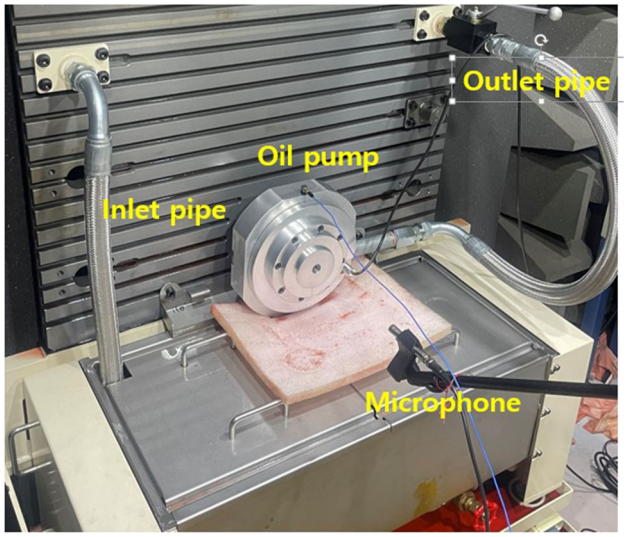

Fig. 25 Experimental apparatus for performance test of oil pump

13.65°) using the results calculated in the automation program, and comparison with lemniscate is shown in Fig. 20. As intended, the chamber width is designed to be relatively wide.

Table 3 compares the performance of the optimal lemniscate teeth developed through the ovoid curve in this study, while the flow pulse and contact stress, which are the performance factors that affect noise, decreased by 0.53% and 14.4%, respectively, while the sliding rate increased by 1.4%. However, according to the experimental data in this laboratory, the lower two performance factors (specific sliding, pressure angle) compared to the upper two performance factors (irregularity, contact stress) have a small effect on the performance of the gerotor. So it can be seen that this is a more suitable tooth shape for pressure pulsation than the existing lemniscate tooth shape.

Considering this cause, in Fig. 21, the area of the wide part of the lemniscate shown in red is 38.49 mm^2, and the area of the narrow part is 3.32 mm^2, so the difference is 35.27 mm^2. The area of the ovoid is 38.46 mm^2 and 6.77 mm^2, respectively, with a difference of 31.69 mm^2, which reduces the deviation of the fluid area compared to the lemniscate. Therefore, it can be seen that as the chamber area is created wider, the deviation of the internal area is reduced, thereby alleviating the flow imbalance.

4.2 Result of CFD

A time-dependent graph illustrating the measured pressure is shown in Fig. 22. In the case of lemniscate, maximum pressure is 1,410,627 and minimum is 798,102pa. And in ovoid, maximum pressure is 1,415,793 and minimum is 816,598pa

The pressure pulsation, difference between the maximum and minimum pressure of the ovoid tooth shape, was confirmed to be 599,195pa. This is an improvement of about 2.22% over 612,524 pa of lemniscate. Therefore, it was confirmed that the pressure pulsation of the ovoid tooth shape was better than that of the lemniscate tooth shape. According to the results of previous studies, the lower the pressure pulsation, the less vibration occurs, improving the noise performance.

To understand why the pressure pulsation was improved, we compared the vorticity magnitude occurring inside the flow field. It can be seen that the wider the chamber is, the lower the curvature of the contact surface of the gear fluid is and the weaker the vortex component is measured. This is expected to affect noise by reducing vibration caused by flow (Fig. 23).

5 Performance test

As a result of theoretical performance parameters and CFD, it was confirmed that the ovoid tooth shape was superior to the existing tooth shape in terms of performance, so an experiment was conducted to verify it. In order to conduct the experiment, the inner rotor, outer rotor, and housing were manufactured as shown in Fig. 24, and they were combined with the experimental equipment as shown in Fig. 25. The gerotor is rotated by the rotational force of the motor. The temperature of the working oil inside the pump is maintained at 85±3°C and the pressure of the outlet part is maintained at $10kg_f/cm^2$. Performance of the new oil pump was compared with that of the existing standard oil pump (2-Ellipses, 2-Ex_Lemniscates) used in the field.

The first parameter measured was the flow rate. The results of flow rate measurements at 1000 to 5000 RPM were compared to existing ones and are presented in Table 4. In all regions except for 1000 RPM, it was observed that the flow rate of the ovoid was higher than that of other tooth shapes. In

Table 4 Comparison of flowrates between 2-Ex_Ovoids and other pumps

	Flow rate (L/min)				
	1000 rpm	2000 rpm	3000 rpm	4000 rpm	5000 rpm
2-Ex_lemniscates	8.73	20.07	32.79	42.97	50.84
2-Ellipses	9.25 (5.9%↑)	20.32 (1.2%↑)	33.52 (2.2%↑)	43.6 (1.5%↑)	51.44 (1.2%↑)
2-Ex_Ovoids	7.79 (10.7%↓)	22.14 (10.5%↑)	33.57 (2.4%↑)	43.76 (1.8%↑)	52.8 (3.9%↑)

Table 5 Comparison of SPLs between 2-Ex_Ovoids and other pumps

	Noise (dB)					
	500 rpm	1000 rpm	2000 rpm	3000 rpm	4000 rpm	Peak
2-Ex_lemniscates	56.93	69.62	79.02	83.94	82.99	85.73
2-Ellipses	50.9 (10.6%↓)	69.28 (0.5%↓)	76.27 (3.5%↓)	84.34 (0.5%↑)	82.3 (0.8%↓)	86.56 (1.0%↑)
2-Ex_Ovoids	53.44 (6.1%↓)	69.37 (0.4%↓)	77.15 (2.4%↓)	80.5 (4.1%↓)	81.57 (1.7%↓)	84.08 (2.0%↓)

comparison to the existing optimal shape, 2-Ex_Lemniscats, it showed an increase of 10.5% at 2000 RPM and 2.4% at 3000 RPM, which are the most commonly used operating ranges.

Next, measurements of sound pressure levels (SPL) were conducted. The noise levels at each RPM ranging from 500 to 4000 RPM were compared as shown in Table 5. It was observed that the developed shape exhibited superior noise performance across all RPM ranges compared to the 2-Ex_Lemniscats. Particularly, a significant reduction in noise was noted at 2000 RPM and 3000 RPM, with reductions of 2.4% and 4.1%, respectively.

6 Conclusion

In this study, we analyzed the impact of performance according to the shape of the georotor for the application of the automobile automatic transmission oil pump (rotor outer diameter, 35 mm), suggested an optimal gerotor profile design based on an oval curve, and confirmed that the optimal gerotor has a high flow rate and sufficiently low pressure pulsation and noise level. Using the dynamic mesh technique, a CFD technique was established for the analysis of flow fields inside two rotating bodies with different rotational axis. Compared to the existing oil pump, the pressure irregularity measured by CFD was improved. Additionally, through experiments, it was confirmed that the new oil pump is superior to performance in terms of both flow rate and noise compared to the existing oil pump. The results of this study are summarized as follows:

(1) Using the ovoid curve as the base of tooth profile of the gerotor a theoretical equation for generating the profile was derived based on Camus' theory. According to the input design variables (flow rate, flow pulsation, pressure angle, contact surface pressure), an automatic calculation program generates various tooth shapes and calculates theoretical performance variables.

- An optimal gerotor with an ovoid curve as a base curve was selected ("d'' = 12.0325 mm, "k_1" = 0.5, "k_2''= 4.4, "η'' = 13.65°) by developing a multi-calculation program.

(2) Through automatic calculation programs and CFD, it was confirmed that the newly developed tooth shape (2-Ex_Ovoids) has superior performance compared to the existing tooth shape.

(3) Through experiment, it was verified that the new oil pump outperforms the conventional oil pump in terms of performance.

- A developed oil pump shows superior noise performance in all RPM ranges compared to the existing one. And, at 2000 RPM and 3000 RPM, it showed reductions of 2.4% and 4.1%, respectively, when compared to the 2-Ex_Lemniscates.

Author Contributions Chanyoung Shin: investigation, formal analysis, conceptualization, methodology, validation, software, writing — original draft; Seungseok Lee: data curation, investigation; Chul Kim: supervision, funding acquisition, writing — review & editing.

Funding This work was supported by Samhan Co., Ltd for funding and technical assistance, and this research was supported by Korea Basic Science Institute (National research Facilities and Equipment Center) grant funded by the Ministry of Education.(grant No. 2021R1A6C101A449).

Declarations

Conflict of interest The authors declare no competing interests.

References

1. Rituraj F, Vacca A (2019) Modelling and validation of tooth tip leakages in gerotor pumps. Fluids Engineering Division Summer Meeting, vol. Volume 1: Fluid Mechanics, pp. 001–01044. https://doi.org/10.1115/AJKFluids2019-5531
2. Lee C, Jang H, Kwak H, Park G, Kim C (2021) Optimal design of gerotor profile with lemniscate lobe shape for noise reduction. Int J Precis Eng Manuf 22(9):1595–1608. https://doi.org/10.1007/s12541-021-00562-6
3. Lee S, Kwak H, Han G, Kim C (2019) Design of gerotor oil pump with 2-expanded cardioids lobe shape for noise reduction. Energies 12(6):1126. https://doi.org/10.3390/en12061126
4. Zhang, N, Li D, Gao B, Ni D, Li Z (2023) Unsteady pressure pulsations in pumps-a review. Energies. 16(1). https://doi.org/10.3390/en16010150
5. Yoon Y, Park B-H, Shim J, Han Y-O, Hong B-J, Yun S-H (2017) Numerical simulation of three-dimensional external gear pump using immersed solid method. Appl Thermal Eng 118:539–550. https://doi.org/10.1016/j.applthermaleng.2017.03.014

6. Gamez-Montero PJ, Castilla R, Codina E, Freire J, Morató, J, Sanchez-Casas E, Flotats I (2017) Geromag: in-house prototype of an innovative sealed, compact and non-shaft-driven gerotor pump with magnetically-driving outer rotor. Energies 10(4). https://doi.org/10.3390/en10040435
7. Cao W, Liu Y, Dong J, Niu Z, Shi Y (2019) Research on pressure pulsation characteristics of gerotor pump for active vibration damping system. IEEE Access 7:116567–116577. https://doi.org/10.1109/ACCESS.2019.2936489
8. Hsieh C-F, Hwang Y-W (2006) Geometric design for a gerotor pump with high area efficiency. J Mech Des 129(12):1269–1277. https://doi.org/10.1115/1.2779887
9. Tessari F, Galluzzi R, Amati N (2019) Efficiency-driven design methodology of gerotor hydraulic units. J Mech Des 142(6):063501. https://doi.org/10.1115/1.4045421
10. Karamooz Ravari FMRMHMR (2012) Flow irregularity and wear optimization in epitrochoidal gerotor pumps. Meccanica 47(4):917–928. https://doi.org/10.1007/s11012-011-9473-6
11. Bonandrini G, Mimmi G, Rottenbacher C (2012) Design and simulation of meshing of a particular internal rotary pump. Mech Mach Theory 49:104–116. https://doi.org/10.1016/j.mechmachtheory.2011.11.001
12. Sang X, Zhou X, Liu X (2015) Performance optimization of an oil ellipse gerotor pump for automotive engine. In: Proceedings of the 5th International Conference on Advanced Design and Manufacturing Engineering, pp. 1686–1690. Atlantis Press